Formation and evolution of metallocene single molecule circuits with direct gold-π links

Journal:	*Journal of the American Chemical Society*
Manuscript ID	ja-2022-01322v.R2
Manuscript Type:	Article
Date Submitted by the Author:	n/a
Complete List of Authors:	Lawson, Brent; Boston University, Physics Zahl, Percy; Brookhaven National Laboratory, Center for Functional Nanomaterials Hybertsen, Mark; Brookhaven National Laboratory, Center for Functional Nanomaterials Kamenetska, Maria; Boston University, Chemistry and Physics

Formation and evolution of metallocene single molecule circuits with direct gold-π links

Brent Lawson,[a] Percy Zahl[b], Mark S. Hybertsen[b,] and Maria Kamenetska [a,c,d,*]*

[a] Department of Physics, Boston University, Boston, Massachusetts, 02215, United States

[b] Center for Functional Nanomaterials, Brookhaven National Laboratory, Upton, New York, 11973, United States.

[c] Department of Chemistry, Boston University, Boston, Massachusetts, 02215, United States

[d] Division of Material Science and Engineering, Boston University, Boston, Massachusetts, 02215, United States

KEYWORDS

Single molecule conductance, Break Junction, organometallics, organometallic interface, atomic resolution

ABSTRACT

Single molecule circuits with group 8 metallocenes are formed without additional linker groups in Scanning Tunnelling Microscope-based break junction (STMBJ) measurements at cryogenic and room temperature conditions with gold (Au) electrodes. We investigate the nature of this direct gold-π binding motif and its affect on molecular conductance and persistence characteristics during junction evolution. The measurement technique under cryogenic conditions tracks molecular plateaus through the full cycle of extension and compression. Analysis reveals

that junction persistence when the metal electrodes are pushed together correlates with whether electrodes are locally sharp or blunt, suggesting distinct scenarios for metallocene junction formation and evolution. The top and bottom surfaces of the "barrel" shaped metallocenes present the electron-rich π system of cyclopentadienyl rings which interacts with the gold electrodes in two distinct ways. An undercoordinated gold atom on a sharp tip forms a donor-acceptor bond to a specific carbon atom in the ring. However, a small, flat patch on a dull tip can bind more strongly to the ring as a whole through Van der Waals interactions. Density functional theory (DFT) based calculations of model electrode structures provide an atomic-scale picture of these scenarios, demonstrating the role of these bonding motifs during junction evolution and showing that the conductance is relatively independent of tip atomic-scale structure. The non-specific interaction of the cyclopentadienyl rings with the electrodes enables extended conductance plateaus, a mechanism distinct from that identified for the more commonly studied, rod-shaped organic molecular wires.

INTRODUCTION

Formation and characterization of single-molecule circuits with organometallic molecules enhance the scope of observable phenomena due to the incorporation of a transition metal atom with new degrees of freedom.[1–4] Metallocenes are a class of such molecules where a metal ion (M) is sandwiched between two cyclopentadienyl rings (Cp). They are synthetically accessible, tunable and stable in a variety of conditions, making them ideal model compounds for these applications. It has been theoretically predicted, and later experimentally observed, that molecular junctions and self-assembled monolayers (SAMs) containing ferrocene (M = Fe) bound to gold through organic linkers exhibit electronic functionality such as current rectification, conductivity enhancement, negative

differential resistance and spin filtration.[5–17] Other metallocenes (M = Ni, V, Co) have also been studied using single molecule methods such as scanning tunneling microscopy (STM) and break junction (BJ) approaches. Similar electron transport properties such as spin filtration, spin sensing and near unity conductance were found to depend on the orientation of the molecule in the junction.[18–21] The sensitivity of conductance phenomena to the physical structure of the nanoscale junction highlights the need for a clear understanding of how these molecules coordinate to the electrodes and for methods to control the metal-molecule interface structure.

Most organic molecules incorporated into single molecule circuits to date closely approximate 1D molecular wire rods with high aspect ratios and specific linker motifs that bind to the electrodes and form the electrical contacts that close the circuit. We have previously demonstrated that junction evolution and conductance of organic molecular wires are sensitive to the atomic shape of the Au electrode and to the length of the molecule between the linking moieties.[22–24] In those junctions, the Au-molecule interface is a localized bond between an Au undercoordinated atom and a single donor atom on the organic molecule, usually a nitrogen (N) or sulfur (S). During junction elongation, the molecular linker can slide along the electrode and change its attachment point on the Au structure, resulting in a flat conductance plateau during pulling over a distance range significantly longer than can be understood from just stretching the link bonds.

In contrast, organometallic compounds such as metallocenes (Fig. 1A), are bulkier with a "barrel" shape. Recently, both vanadocene (M = V) and nickelocene (M = Ni), studied by STM, have been found to bind to metal electrodes either through the metal atom for vanadocene (Au-M-Au) or through the Cp ring (Au-Cp-M-Cp-Au) for nickelocene and

vanadocene.[20,21,25] Metallocenes can also be extended with specific functional linker groups to direct the anchor point to the gold as demonstrated in some conductance studies.[9,14,26,27] Significantly, the metallocenes as such offer a distinctive feature, the delocalized electrons on the Cp rings that can coordinate to the electrodes. This aspect is emphasized by the electrostatic potential map of the molecule in Fig. 1A which shows increased electron density on the flat Cp ends of the "barrel" and relatively decreased density along the sides of the molecule. We hypothesize that formation and evolution of molecular junctions with "barrel" shaped organometallic molecules, without functional linker groups, follow scenarios dictated by the electron-rich rings and the atomic-scale shape of the metal electrodes.

Specifically, we investigate the geometry, conductance and evolution of molecular junctions made with group 8 metallocenes (M=Fe (**1**), Ru (**2**), Os (**3**)) on gold, as shown in Fig. 1A. These closed-shell, barrel-shaped molecules serve as a convenient test case for studying atomic arrangements and evolution of molecular junctions with organometallic molecules containing multihaptic ligands forming a 3D structure rather than a 1D rod. Here, using Scanning Tunneling Microscope break junction (STMBJ) conductance measurements in cryogenic and room temperature conditions, we show that the metallocenes form reproducible metal-molecule-metal junctions despite a lack of coordinated linker groups such as amines or thiols. At 5 K in vacuum, we measure and correlate the conductance evolution of each junction during pushing and pulling to the shape of the electrodes deduced from the measured electrode snapback distance. Supported by DFT based calculations of junction structure and conductance as a function of tip-sample distance, we find that the metallocenes bind primarily through the electron-rich

cyclopentadiene (Cp) conjugated moieties on both sides of the molecule. In addition to bonding between undercoordinated Au atoms and specific C atoms of the Cp rings, we find a significant, additional role for binding of the barrel shape molecule to flatter binding areas exposed on blunt electrodes, promoted by van der Waals interactions.

EXPERIMENTAL SECTION

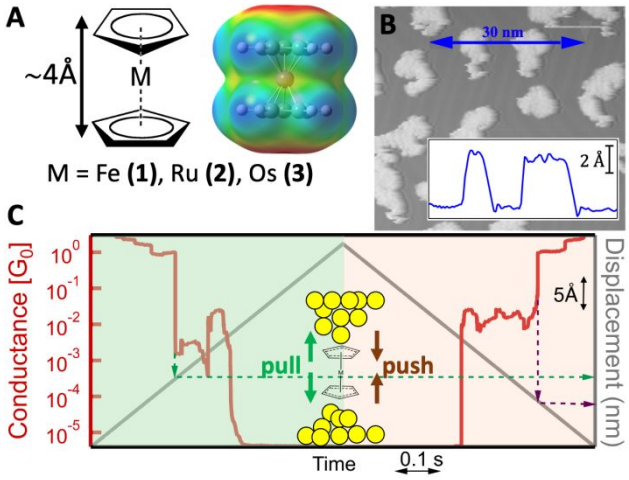

Fig. 1 (A) Structure of Group 8 metallocenes: ferrocene (**1**), ruthenocene (**2**), and osmocene(**3**). Also shown is a ball-and-stick model of ferrocene with a constant charge density contour color-coded to the electrostatic potential, indicating electron rich (red) and electron deficient (blue) regions. (B) STM image and height profile (inset) of submonolayer clusters of ferrocene deposited on Au(111) at 5 K. (C) Conductance trace measured in the presence of ferrocene on the Au(111) surface while pulling the tip out of contact with the surface and then pushing the tip back in to contact. The snapback distance is calculated from the difference in the displacement (grey) at the points when the tip breaks and reforms contact, as indicated by the dashed arrows.

Molecular Deposition and Measurements in Cryogenic Conditions

We perform single molecule conductance measurements in ultra-high vacuum using a commercial STM (Createc) with custom control hard and software GXSM at the Center for Functional Nanomaterials at Brookhaven National Laboratory.[28,29] The low temperature STM break junction (LT-STMBJ) measurements are performed at 5 K and less than 10^{-10}

mbar. We repeatedly form and break quantum point contacts in the presence of a sub-monolayer of molecules. Metallocenes are deposited on atomically flat Au(111). A clean surface is achieved through two cycles of sputtering and annealing of a single crystal gold sample according to standard methods.[30] To create the sub-monolayer, we expose the Au (111) surface at 5 K to a ~10^{-7} mbar vapor pressure of either ferrocene (**1**) (CAS: 102-54-5) or ruthenocene (**2**) (CAS: 1287-13-4) molecules sublimed at room temperature in the preparation chamber of the STM under base pressure of 10^{-10} mbar for 30 seconds. All gold tips are formed by mechanically cutting a 0.35 mm wire purchased from Fisher Scientific (99.99% metals basis for Au). STM images of both **1** (Fig. 1B) and **2** on Au(111) are taken at 0.7 V bias in Gain 9 to verify sub-monolayer formation. The height profile of molecular islands, shown in Fig. 1B, is measured to be 3.5 Å which is in good agreement with the long axis of the molecule and consistent with a sub-monolayer of **1** adsorbed on the Au(111) surface.[31] We do not observe dissociation of **1** or **2** on the surface under the mild imaging conditions used here.[31–33]

Break junction measurements are performed both on the clean Au(111) sample prior to the vapor deposition and on the sample with a sub-monolayer coverage of metallocenes. For LT-STMBJ measurements, we record current between a gold tip and substrate under constant bias of 50 mV while displacing the tip relative to the substrate with sub-Angstrom resolution. To maximize the dynamic range of our measurement, we use a log amplifier (part #AD8304). Our break junction measurement consists of a repeated series of tip pulls and pushes. Using STM imaging, we first locate an unperturbed region of the surface with sub-monolayer coverage of molecules such as the one shown in Fig. 1B. Then, we position the tip a few nm above the surface by adjusting the set point current under 50 mV bias. We then initiate an automated protocol to

collect 1000's of conductance vs displacement curves. The protocol establishes tip-sample contact by smashing the tip to a conductance > $1G_0$, and then successively pulls and pushes the tip in and out of the sample by 4 nm as shown. We perform this pull-push motion 10 times in the same location. Then we displace the tip by several nanometers laterally to access a new area of the surface and repeat the pull-push protocol. Overall, this cycle is repeated hundreds of times to acquire the full data set.

A single conductance trace measured at 5 K as a function of tip displacement during junction pulling and pushing is shown in Fig. 1C. Both pull and push portions of the trace display plateaus at multiples of G_0, allowing us to identify the displacement coordinates along the trace (dashed arrows in Fig. 1C) where the gold quantum point contact breaks and reforms respectively. To measure the snapback distance, we determine the distance between the electrodes immediately after rupture relative to when the electrodes come back into electrical contract during push and the conductance jumps to near G_0 as shown in Fig. 1C. At the latter point, the inter-electrode distance is taken to be nominally 0 Å.[34] Physically, the centers of the apex atoms on the tip and sample are approximately separated by 2.5 Å, the diameter of Au atoms.[23,35] This analysis ignores jump-to-contact which can occur during junction closing. While this affects our snapback distance measurements, the scale of the jump-to-contact effect (up to 1 Å) is significantly smaller than the snap-back range observed here.[36]

Room Temperature Break Junction measurements

Room temperature measurements are performed using previously described protocols.[22,23,37] Briefly, we repeatedly break and reform quantum point contacts of gold in a solution of molecules at standard temperature and pressure while recording the junction conductance and relative displacement. We form our gold tips by mechanically cutting 0.25 mm wire purchased from Fisher

Scientific (#AA14730BY 99.999% metals basis). To make Au samples, we polish metal specimen disks (Ted Pella #16219) and then coat the samples with 150 nm of gold (Fisher Scientific #AA14726BS, 99.999% metals basis) in a thermal evaporator. All measurements are done in a 1 mM or less solution in 1,2,4 Trichlorobenzene (Sigma Aldrich #296104), a nonpolar solvent. Data collection and processing is automated with a home-built Wavemetrics Igor Pro code. All measurements are done at 100 mV bias, with a relative tip-sample speed of ~20 nm/s.

Data Analysis

To analyze the formation, evolution and conductance of metallocene junctions with statistical significance, we collect and bin push and pull traces in corresponding push and pull logarithmically-binned conductance histograms.[22,23,37] To create log-binned 1D conductance histograms, the logarithm of conductance values along hundreds (5 K) or thousands (room temperature) of conductance traces are binned into equally-spaced bins. For 5 K measurements, traces without pronounced 1 G_0 plateaus or molecular features may be filtered out using well-established approaches, as described in the SI.[38,39] Recently, several data analytics techniques have been demonstrated for unsupervised clustering of experimental traces, distinguishing traces with molecular features as such as well as different classes of molecular junction structure.[40–42] In the present study, identification of traces with molecular features did not prove to be ambiguous. The analysis of molecular junction structure discussed below is based on physically measured descriptors.

To create 2D conductance versus tip displacement histograms, we identify the point where Au junction ruptures (for pull) or reforms (for push) in each trace as the zero of displacement. Individual traces are added up into histograms with linear bins along the displacement axis using this common distance origin. The conductance is binned logarithmically as for 1D histograms.

The resulting 2D heat maps demonstrate the average evolution of junction conductance with changing tip-sample distance, shown for **1** and **2** in Fig. 2A-D. As has been established previously, for pull histograms, the zero on the displacement axis may correspond to a range of inter-electrode distances depending on the snapback value. In contrast, for push histograms, the origin of the displacement axis corresponds to a point where the inter-electrode distance is nominally 0 Å, as defined above. The data sets are also presented as conventional logarithmically-binned 1D histograms as shown in Fig. 2E-F.

Density Functional Theory Calculations

All DFT calculations are performed with the FHI-aims suite to obtain total energy, relaxed atomic-scale structure, and electronic structure. The non-equilibrium Green function method is used for calculating electron transmission through specific models for nanoscale junctions, as implemented in the AITRANSS package.[43–47] Various geometries of different gold electrodes with either **1** or **2** are relaxed using the PBE exchange correlation functional and Van der Waals corrections (Tkatchenko-Scheffler). The Kohn-Sham states are computed with an all-electron, atom-centered basis set. The FHI-aims suite supplies several options for optimized, numerical basis sets. Final results were computed using the "tight" level (similar to double zeta plus polarization) for the atoms in the molecule and the "loose" level (double zeta) for the Au atoms in the electrodes.[48,49] The size of the gold structures used to model gold electrodes is converged with increasing number of gold atoms. The final calculations are performed with at least 18 atoms per electrode, with adaptations to model different features of the tip structure (sharp versus blunt). In these calculations the positions of the atoms in the molecule and two apex layers of gold atoms on each electrode are allowed to relax. Relaxation was considered complete when all force

components/atom were less than 10^{-2} eV/Å. Charge transfer calculations are performed and checked for convergence within FHI-aims using a Mulliken population analysis.

We simulate the pushing and pulling process in the break junction measurements by moving the electrodes in or out in steps of 0.15 Å or less and then relaxing the complete structure. For each step in the calculated trajectory, the interaction energy is the energy difference between the relaxed junction structure and the relaxed components (the two electrodes and the metallocene molecule). The transmission spectra across the molecular junction as a function of energy at zero bias for each step is calculated using AITRANSS.[45,46] We also compute the transmission for model junction structures without molecules present. To establish the reference electrode separation, we determine the electrode separation where the calculated transmission crosses 1 G_0 and designate that reference separation to be 0 Å, parallel to the convention used for the experimental push trajectories as described above. This approach allows us to compare the calculated distances to the experimentally measured Au-Au distances plotted in push 2D histograms.

RESULTS AND DISCUSSION

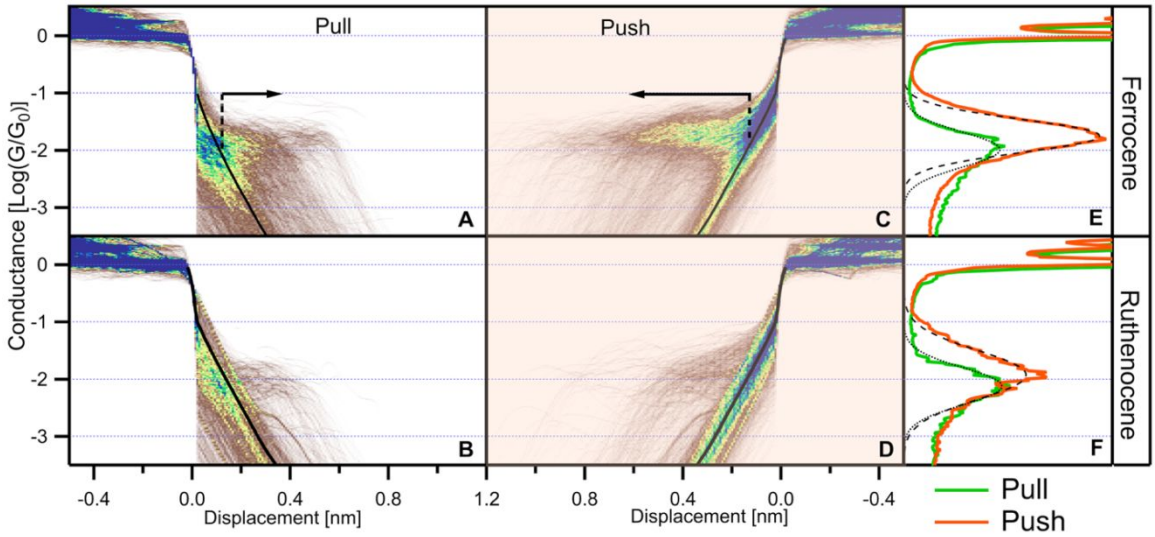

Fig. 2 (A, B) 2D conductance vs displacement for ferrocene (A) and ruthenocene (B) on Au(111) constructed from pull traces (tip withdrawal). **(C, D)** 2D conductance vs Au-Au separation for ferrocene (C) and ruthenocene (D) on Au(111) constructed from push traces (tip approach). The solid black lines are exponential fits to the clean Au pull and push data in Figure 1S and indicate the average tunnelling current evolution on clean gold. For conductance values corresponding to the most probable values in the histograms (E), arrows indicate an extension beyond the Au separation for vacuum tunnelling by 2 Å in (A) and 5 Å in (C). **(E, F)** 1D conductance histograms constructed with the push and pull traces separately for ferrocene (**E**) and ruthenocene (**F**). Traces that do not exhibit a molecular plateau are filtered out in (**E**) and (**F**) only.

Experimental Measurements

The data collected at 5 K for ferrocene and ruthenocene are summarized in Fig. 2. For these histograms, all traces that displayed a pronounced 1 G_0 feature during pull were included (details in the SI). The exponentially decaying signature (black lines in Fig. 2A-D) in the histograms is due to tunneling background through vacuum and is also observed on clean gold traces (Fig. S1).[24] In addition, we observe molecular conductance plateaus in the range from ~0.005 G_0 to ~0.08 G_0, attributable to the formation of ferrocene and ruthenocene junctions during both the pull and push portions of the cycle. We determine that ~30% of pull and ~40% of push traces measured in the presence of **1** and ~20% of traces in the presence of **2** (Table S1, after filtering for poor tips), display molecular conductance features below 1 G_0. For comparison, we note that ethanediamine

is a saturated molecular wire with a similar length to ferrocene of 3.8 Å (N-N distance) and a conductance of ~0.005 G_0. On pull, this molecule is found to bridge ~25% of junctions.[22]

We focus in on metallocenes junction properties by filtering out traces with no molecular signature. This eliminates the background counts in the histograms that arise from the exponentially decaying tunneling current in junctions that are not bridged by a molecule. We then construct filtered 1D log-binned histograms. As shown in Fig. 2E and F, the resulting 1D histograms for both **1** and **2** display a more prominent molecular conductance peak for the push traces than for the pull traces. We determine the most probable conductance, histogram peak position, for the push (pull) signal: 0.017 (0.010) G_0 and 0.011 (0.008) G_0 for **1** and **2** respectively. While the most probable conductance for **2** is 30-40% smaller than for **1**, these differences are smaller than the widths of the histograms and suggest that transport in group 8 metallocenes does not depend strongly on the metal center.

To compare the persistence statistics of molecular plateaus we turn back to the 2D histograms for **1** in Fig. 2A and C. At the pull conductance value of 0.010 G_0 (1D histogram peak), the average molecular plateau extends ~2 Å (length of the arrow in Fig. 2A) past the tunneling background to where the Au-Au distance is ~4 Å, comparable to the length of the molecule. In contrast, at the push conductance of .017 G_0 (1D histogram peak), molecular signatures extend at least 5 Å (length of arrow in Fig. 2C) past tunneling. Furthermore, the distribution of traces includes junctions in which the molecular conductance signature remains for Au-Au separation of more than ~8 Å. This characteristic of more extended molecular signatures during the push for metallocenes is distinct from previous results for junctions formed with organic molecular wires linked to Au by amine or thiomethyl groups in cryogenic conditions.[24,25,50]

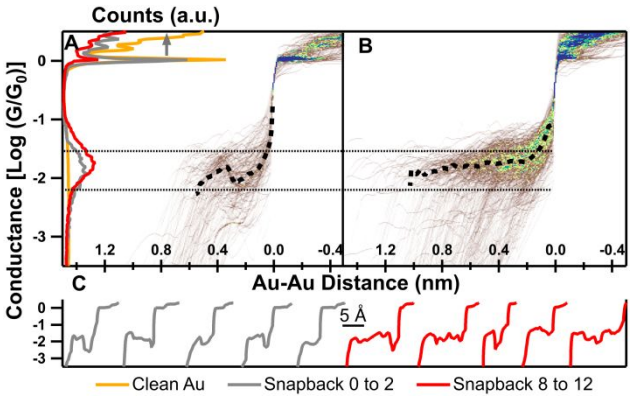

Fig. 3 (A) Left: 1D conductance histogram of clean Au push traces (orange) and the ferrocene push traces filtered by snapback distance ranges of 0 to 2 Å (gray) and 8 to 12 Å (red). **Main panel:** 2D conductance vs inter-electrode distance histogram of ferrocene push traces with a snapback distance between 0 and 2 Å. **(B)** As in (A), but with snapback distance between 8 and 12 Å. Heavy dashed lines (black) in (A) and (B) indicate the most probable conductance at each distance. Light dash lines mark the half-sigma range around the most probable conductance from the 1D histogram at left. **(C)** Five selected traces for each case (0 to 2 Å, grey; 8 to 12 Å, red).

To probe metallocene binding geometry and persistence in the junction, we examine the occurrence and step length of the ferrocene molecular junctions as a function of electrode snapback and 1 G_0 step length. For each pull-push trace, we use an automated protocol to calculate the snapback as illustrated in Fig. 1C. The 5 K snapback distribution determined for the present dataset is shown in Fig. S3 and agrees with previous measurements.[22,24,35,51] We observe that the snapback distribution is roughly quantized in multiples of a gold atom lengths.[52] Furthermore, Fig. 4S A and C illustrates that traces with longer snapbacks on average display longer 1 G_0 plateaus during the pull.[51] This pattern is consistent with the accepted view in the field that a gold atom chain containing an integer number of gold atoms can be pulled out during the stretch portion of the cycle. The chain eventually collapses leading to 1 G_0 rupture and a nanogap between the two electrodes.[51–54] The length of this snapback has been previously shown to correlate strongly with electrode geometry. Snapback values less than 2 Å are characteristic of Au electrodes that do not undergo significant plastic deformations and retain their atomically sharp structure after rupture.[24,36] Larger snapback values, characteristically >8 Å, are associated with rearrangement of the apex atoms that collapses the electrodes into a flatter structure after 1 G_0 rupture.[24,54]

We sort traces that exhibit a molecular conductance signature based on the snapback determined for each pull-push trace. The data is sorted into bins based on snapback (Table S2). Then 1D and 2D push and pull histograms are created for specified ranges of snapback distance. The full set of push data for **1** is shown in Fig. S5. The 1D push histograms plotted in Fig. S5A (top axis) confirm that the longest snapback traces >8 Å corresponding to 3 or more Au gold atom diameters (red) have a significantly diminished 1 G_0 peak. These trends are also evident in correlation plots shown in Fig. S4 C, D where traces with longer snapback are found to have shorter 1 G_0 plateaus. This result indicates that these traces form larger-area metallic contacts upon being pushed together.[24,53] In the discussion below, we will term these 'blunt electrodes.' We note that 'blunt electrodes' may also include electrodes whose pointed tips are displaced laterally relative to each other. In these cases, the shortest distance between the electrodes where the molecules might bind is still flanked by flat metal faces and the 'blunt' designation applies, albeit with a different orientation for the flat region. In contrast, the histogram constructed from traces with short snapback shorter than 2 Å (gray), less than the diameter of a gold atom, displays a prominent 1 G_0 peak. This indicates a lack of atomic reorganization upon $1G_0$ rupture and much higher probability for protruding gold atoms on the electrodes in this case to be pushed together to form a single atom contact. We will refer to these as 'sharp electrodes.'

Focusing now on the 2D histograms of molecular signatures in Fig. S5, we observe that the length of the molecular plateaus, on average, increases with increasing snapback. The shortest plateaus occur on the sharp electrodes in Fig. S5A; a mix of short and long molecular plateau lengths is observed in intermediate snapback regimes (Fig. S5B-C) which form the bulk of experimentally observed traces. Finally, the longest molecular plateaus, are observed on the blunt

plateaus (Fig. S5D). Here we focus on the sharp and blunt extrema of the distribution, reproduced in Fig 3 for **1** and Fig S6 for **2**. This provides clear contrast between physical scenarios.

We compare the evolution of junctions during pushing on the sharp (Fig. 3A) and blunt (Fig. 3B) electrodes. The most probable conductance, determined at each junction elongation, is indicated by the dashed black line on Fig. 3A and B. In both cases, starting from the noise floor, as the electrodes are pushed together, the conductance initially increases exponentially and then transitions to a plateau. At sufficiently small electrode separation, it rapidly increases towards 1 G_0, with a profile characteristic of direct tunneling between the electrodes and reformation of Au-Au contact (Fig 2C-D).

We observe specific differences depending on the snapback regime. Upon pushing sharp electrodes together (small snapback), the molecular regime starts at Au-Au separation of ~5 Å and persists within half of a standard deviation from the most likely conductance (gray dotted lines) for ~2 Å. This is followed by a drop in conductance at ~3 Å Au-Au separation. On the other hand, for blunt electrodes (large snapback), the molecular regime starts at an Au-Au separation of ~10 Å and persists down to ~2 Å. There is no dip seen in the most probable conductance profile. Remarkably, the most likely conductance we observe at Au-Au separation of ~2 Å is unchanged from that at ~10 Å. These distinct effects are evident in individual push traces shown in Fig. 3C. For sharp electrodes, the molecular plateau length is roughly ~2 Å and a dip typically occurs before the rapid rise and Au-Au direct contact formation. For blunt electrodes, the plateau length is generally longer. While a dip occurs in some traces, others display a smooth conductance transition from the molecular conductance plateau to the rapid rise towards 1 G_0. Statistically, the latter evidently dominate.

Conductance trajectories during pushing for **2** exhibit a qualitatively similar behavior, as shown in Fig. S6. Molecular plateaus are longer on blunt electrodes than on sharp ones, which display a relative dip in conductance prior to 1 G_0 contact formation. We note that the smaller dataset collected with **2**, results in greater statistical fluctuation in the average junction evolution behavior with **2**.

In comparison, the 2D pull histograms sorted by snapback for **1** (Fig. S7) and **2** (Fig. S8) show only a modest difference in persistence. The 2D histograms for the subsets of the data selected for small and large snapback are similar to each other as well as to 2D histogram for the full data set (Fig. S2). This trend is also evident in Fig. S9, which shows that molecular plateau lengths for the pull portion remain on average constant with increasing snapback distance in contrast to push molecular plateaus which tend to increase in length as snapback increases. Figure S10 demonstrates that, although pull and push molecular plateaus tend to occur in the same trace due to the spatial clustering of molecules shown in Figure 1B, the distribution of push molecular plateau lengths is statistically independent of the co-occurrence of a pull plateau in the same pull-push cycle. This fact emphasizes the distinct evolution of ferrocene junctions during the opening and closing parts of cycle with the same set of electrode tips.

A smaller fraction of traces with molecular plateaus on the pull compared to the push portion of the measurement prevents robust statistical analysis of small length differences in pull traces observed here. On the other hand, it is clear that overall, the pull histograms in Fig. 2A-B, exhibit a similar molecular plateau persistence to the push histograms for sharp tips. This suggests similar bonding motifs for junction formation in these cases.

The ~2 Å persistence length we observe for pull traces and for push traces with sharp electrodes corresponds roughly to the length of donor-acceptor bonds between gold and organic molecules

reported in the literature.[30,55] Furthermore, the dip in the push traces suggests that the probability of junction rupture increases significantly when the Au-Au distance is shorter than ~3 Å, comparable to the size of the molecule. The minority of traces with longer plateaus indicate more complex evolution of the junction structure. In contrast, for push traces on dull electrodes, the average conductance is slightly higher, and the molecule can remain bound as the junction is compressed over ~8 Å in length. Furthermore, that conductance is maintained, on average down to the Au-Au distance where direct inter-electrode interactions become significant. The constant conductance plateaus which exceed the length of the molecule upon pushing on blunt electrodes suggests junction evolution trajectories where the molecular binding and electron transport is relatively insensitive to Au-Au distance. In fact, this phenomenon of constant molecular conductance over multiple Angstroms of compressing is reproduced on all but the most atomically sharp tips (snapback shorter than 2 Å) in our dataset as can be seen in Fig. S5B-D.

We perform room temperature, pull conductance measurements on molecules **1-3** as described in the methods section. Push measurements at RT conditions do not result in reproducible molecular signatures.[23] We also do not obtain a reliable pull conductance histogram of **1** at RT conditions. This result may be due to lower solubility of this molecule in the nonpolar solvent used here compared to **2** and **3** or to its slightly shorter length which may decrease its binding probability under RT junction formation conditions. 2D histograms of 4000 traces each of **2** and **3** measured in solution at room temperature during pull are shown in Fig. S11. We observe similar conductance signatures for **3** compared to **2**, with average conductance values of 0.0009 G_0 and 0.0008 G_0 respectively. This result reinforces the conclusion from cryogenic measurements above that the nature of the metal ion does not affect transport through group 8 metallocenes.

Comparing RT with cryogenic measurements, we observe a lower conductance for **2** at RT (0.0009 G_0) compared to 5 K (0.008 G_0). We note the conductance peaks in 5 K and RT 1D histograms are both more than 1 order of magnitude wide, making the comparison of average conductance values less meaningful. The histograms for **2** measured at RT and 5 K do overlap, with significant counts falling between 10^{-2} and 10^{-3} G_0. The effect of temperature on average molecular junction conductance has been documented previously. Electrode geometries vary significantly with temperature.[24] Metal-molecule energy level alignment, dynamics of junction relaxation, and other details of junction formation and transport have been attributed to thermal effects. These considerations as well as solvation effects in RT measurements can result in complex dependence of transport on junction environment.[24,50,56,57]

DFT Calculations

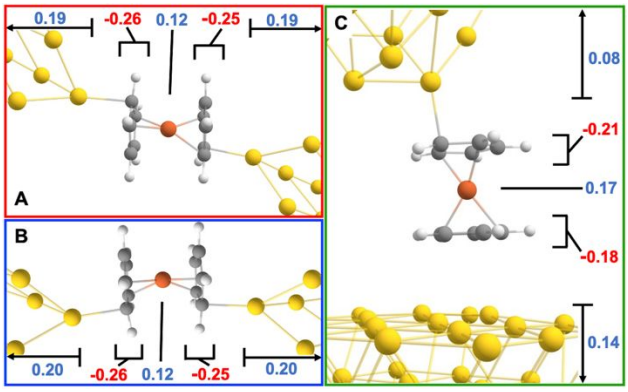

Fig. 4 Calculated relaxed geometries for ferrocene bound to gold electrodes in three distinct junction motifs at a tip separation corresponding to the potential energy minimum and the corresponding charge transfer induced by bonding of the ferrocene to the electrodes. (**A**, red) Ferrocene bound to sharp electrodes in a trans geometry. (**B**, blue) Ferrocene bound to sharp electrodes in a cis geometry. (**C**, green) Ferrocene bound to dull electrodes. Numbers report the net change in Mulliken population in each indicated slice of the junction structure.

To further understand our results, we investigate the electronic properties of the group 8 metallocenes and consider representative scenarios for junction formation, evolution, and the associated electronic transport. The qualitative features of the frontier electronic states of an

isolated ferrocene molecule have long been understood from the interplay between the π-states on the Cp rings and the d-states on the central Fe.[58–60] Our DFT calculations in the minimum energy eclipsed conformation agree with previous results and allow us to visualize the trends in the frontier orbitals showing the combinations of the Fe 3d and the Cp π orbitals (Fig. S12).[61,62] The HOMO and HOMO-1 are degenerate with $3d_{x^2-y^2}$ and $3d_{xy}$ character on the Fe while the HOMO-2 exhibits $3d_{z^2}$ character. The LUMO and LUMO+1 which are also degenerate, are identifiable from their $3d_{xz}$ and $3d_{yz}$ distributions on the Fe atom. Qualitatively, the occupied frontier orbitals have more weight on the central Fe while the empty orbitals have more weight on the Cp π orbitals. The calculated DFT orbital energies, ionization potential (IP), and electron affinity (EA) for **1** (Table S3), all suggest that the HOMO is closer to the Fermi energy of the electrodes. In comparison, for ruthenocene (**2**), the HOMO-LUMO gap and the IP are larger (Table S3), consistent with our observation of somewhat smaller conductance (Fig. 2).

To investigate the possible binding configurations of metallocenes in Au junctions, we relax junction structures with **1** on both sharp (Fig. 4A and B) and blunt (Fig. 4C) electrode models. The blunt electrode model is asymmetrical with one electrode modeled by removing an apex atom and the other by a flat 4x5 Au atoms slab. A third scenario could involve two flat electrodes. However, the longest snapbacks we observe in the experiment are on the scale of 4 Au atom diameters (Figure S3), suggesting that the amount of reorganization during snapback would be unlikely to generate two flat electrodes. We find several binding geometries, as shown in Fig. 4, with energies exceeding 0.5 eV per bond where the Cp ring contacts metal electrodes. The structures shown correspond to local energy minima as a function of electrode separation, as we discuss further below. On sharp electrodes we observe stable binding in both the trans (red) and the cis (blue) configurations as shown.

To understand the effect of the electrode binding on the electronic structure of the molecule, we first calculate the change in electron density that occurs upon binding using a Mulliken population analysis. As seen in Fig. 4, in all bridging configurations considered here, there is net electron transfer from the ferrocene to the electrodes, consistent with expectations for the interaction between the electron rich Cp rings and gold. In the sharp electrode case, (red and blue), more net charge is transferred from the molecule to the gold. Self consistently, the central Fe atom also gains electron density, with a greater transfer on blunt electrodes. For the sharp electrodes, this is indicative of donor-acceptor bonding to undercoordinated gold atoms on the electrodes. The Au-C bond distance found here of 2.35 Å is consistent with this interpretation. For the blunt electrode, the magnitude of charge transfer is similar to that found in studies of ferrocene and nickelocene on copper surfaces.[63,64] In agreement with that prior work, we find that Van der Waals interactions play an important role in molecule-surface binding. We note that in the blunt case, the binding energy is higher than on sharp electrodes by 0.2 eV per electrode, while the Au-Cp distance is about 1 Å longer than Au-C donor-acceptor bond length.

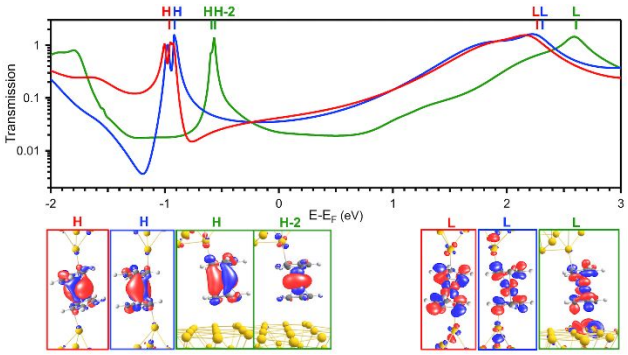

Fig. 5 Calculated transmission spectrum for each of the three junction structures illustrated in Fig. 4: Sharp electrodes, trans (red); sharp electrodes, cis (blue); and dull electrodes (green). Bottom: Isosurface plots of molecular orbitals for the dominant eigenstates related to transmission. Labels of HOMO (H), HOMO-2 (H-2) and LUMO (L) indicate the isolated ferrocene orbitals which dominate at the indicated transmission maxima.

We calculate the electron transmission through these molecular junctions as a function of electron energy to understand how the binding geometry and the resulting charge transfer affect

electron transport. Transmission results are shown in Fig. 5 for each of the junction structures illustrated in Fig. 4. Overall, the resonances associated with occupied frontier molecular orbitals are closer to the Fermi energy than those that derive from the empty molecular orbitals. However, the latter exhibit stronger electronic coupling to the electronic states of the electrodes, as indicated by the larger width of the resonances. This is consistent with the relatively larger weight of the LUMO states on the Cp π orbitals of the isolated molecules (Fig. S12). We note also that the greater charge transfer from the molecule to the gold in the sharp electrode case leads to a shift to lower energies of the molecular spectrum relative to the Fermi energy which will affect the dominant transport channel as we discuss below.

Isosurface plots of key frontier orbitals for molecules coupled self-consistently to the electrodes in each junction structure are shown in Fig. 5. For the blunt electrodes, near degenerate molecular HOMO and HOMO-1 ($3d_{x^2-y^2}$ and $3d_{xy}$) and HOMO-2 ($3d_{z^2}$) contribute to the primary resonances near -0.5 eV. In the junctions with sharp electrodes, the near degenerate orbitals with $3d_{x^2-y^2}$ and $3d_{xy}$ character contribute, but not the $3d_{z^2}$. In all three junctions, the transmission spectra exhibit a characteristic asymmetric peak shape due to interference (Fano) effects among these channels. For the two junctions formed from sharp tips, the trans versus cis bonding configuration in the junction leads to asymmetry with broader shape to the lower versus the higher energy side of the transmission peak.

Focusing on the transmission near the Fermi energy, the transmission has a negative slope in the case of the blunt electrodes, indicating that occupied state mediated tunneling dominates. The transmission for the junctions with sharp electrodes shows the opposite, corresponding to empty state mediated tunneling. Several factors contribute to this contrasting behavior. First, for the sharp electrodes, the main resonances are shifted down in energy relative to the Fermi energy due

to the increased charge transfer from the molecule to the gold as was described previously. This factor, combined with the stronger coupling of the empty molecular states to the electrodes results in "LUMO" dominated transport. Second, for the blunt electrodes, the HOMO are higher in energy relative to E_F and the asymmetric lineshape is broader on the high energy side. Taken together, this leads to "HOMO" dominated tunneling for the blunt electrodes.

Despite these differences, in all three cases, the transmission at the Fermi energy is found to be in the relatively narrow range of 2 to 4 $\times 10^{-2}$ G_0, independent of whether it is HOMO or LUMO dominated. It is also similar for sharp and blunt electrodes. The calculated conductance magnitude is a bit larger than the measured range. This is fully consistent with the trend that is broadly observed when comparing DFT-based transmission to measured conductance for single molecule junctions.[65–69] Corrections to the DFT-based approach[69] or consideration of the additional screening due to neighboring molecules[24] or a solvent[70] can affect the level alignment and the magnitude of the calculated conductance.

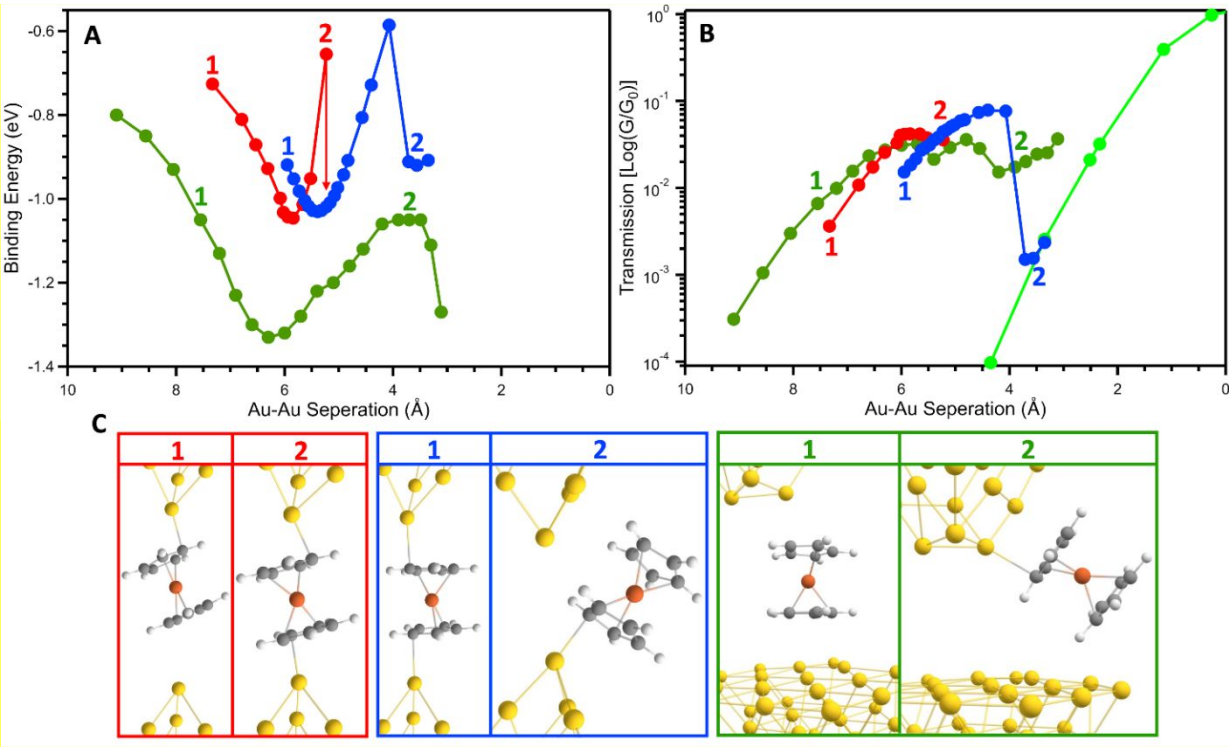

Fig. 6 (A) Binding energy calculated for ferrocene bound to sharp electrodes in trans configuration (red), to sharp electrodes in cis configuration (blue) and to dull electrodes (green) versus electrode separation as the electrodes are pushed together. **(B)** Calculated transmission versus electrode separation for each junction structure on the three trajectories shown in (A) and for a model of Au electrodes without ferrocene (neon) as a reference. The structure of the clean Au junction is shown in Fig S9 of the Supplement. **(C)** Ball-and-stick figures showing junction structure for the numbered snapshots from the trajectories in (A).

Next, we investigate whether this invariance of conductance to geometry can result in the extended junction plateaus measured experimentally upon pushing junctions together. We consider the evolution of the three sharp and blunt ferrocene junction structures in Fig. 4 as a function of Au-Au separation. We specifically model push trajectories, starting with a larger Au-Au separation (relative to the examples illustrated in Fig. 4) and decreasing the separation in small steps as described in the methods section. We plot the resulting binding energy and transmission at the Fermi energy in Fig. 6A and 6B respectively. We note that the 0 Å on the Au-Au separation axis for our calculated geometries corresponds to the point when electrodes come into electrical contact, just as in our experimental data in Fig. 2 and 3, allowing us to compare the plots directly. Representative junction snapshots are shown in Fig. 6C.

We observe that the Cp-bound trans configuration (red) is most stable at ~5.5 Å of tip-tip separation, where the molecule is fully elongated and tilted in the junction to bind to gold electrodes through the two most distant carbons on the opposite Cp rings. Upon compression, at about ~5.1 Å of tip-sample distance as shown by the arrow, the electrode changes attachment site on the Cp ring of the molecule and switches to the cis configuration (blue). In this configuration, the most proximal carbons on opposite Cp rings are bound and the junction can accommodate the shrinking distance. As seen in Fig. 6B, this change in junction structure does not appreciably affect the calculated conductance. Finally, at ~4 Å of displacement, the molecule breaks contact with the bottom electrode and rotates out of the junction. The concomitant decrease of conductance to the tunneling regime at this inter-electrode distance, seen in Fig. 6B, indicates that the molecule no longer provides a tunneling pathway. Taken together, the combined trajectory calculated for sharp electrodes predicts a conductance plateau extending from ~6 to ~4 Å of Au-Au displacement, followed by a dip in conductance upon further compression.

Studies of junctions formed from vanadocene with Ag electrodes indicated an alternative junction geometry for sharp electrodes, with the electrode tip atoms directly coupled to the central metal atom of the metallocene. Our computed junction evolution with Au tip atoms directly coordinating the Fe atom is shown in Fig. S13. The junction binding energy over the range of electrode separation from ~6 to ~4 Å is similar to that found for the Au-C bonded junctions. However, as the electrodes are further pushed together, the ferrocene is shifted aside leaving an increasing role for direct Au-Au interaction between the electrodes. The junction energy continues to drop as a consequence and the conductance crosses over to a regime more characteristic of direct tunneling between the electrodes. As a results, no drop in conductance prior to $1G_0$ contact is observed for this geometry.

The computed trajectory for our model of ferrocene junction formation with blunt electrodes (green traces in Fig. 6) shows a deeper and broader energy curve and correspondingly a wider plateau in the conductance as compared to the models for the sharp electrode. Nearly identical energy and conductance trajectories are found for the molecule initially bound to the flat surface or the blunt pyramid. Despite the longer equilibrium Au-Cp distance of these van der Waals-bound junctions mentioned earlier, the most stable binding energy on these blunt electrodes is ~20% more than found for models of sharp electrodes where the binding is consistent with donor-acceptor bonding. As the junction is further compressed, the metallocene progressively tilts and slides along the flat surface to accommodate the decreasing inter-electrode separation. Surprisingly, even as the molecule tilts from the vertical by more than 60°, the binding energy decreases modestly, while the conductance remains virtually unchanged. Overall, the computed conductance rises from the tunneling regime, crossing over to form a molecular conductance plateau at ~7.5 Å that persists until the direct Au-Au tunneling path takes over as the electrodes reach ~3 Å separation. The computed tunneling conductance in the latter regime is larger than that computed for a single Au atom point contact. The upper tip in the blunt electrode structure naturally approaches a contact area with three Au atoms.

Discussion

Together, our experimental results, analysis and computational results for model junction structures provide a clear picture for molecular junction formation and conductance characteristics with group 8 metallocenes. The experimental methodology in this study where the junction is tracked continuously through a full cycle of pull and push enables correlation of conductance properties to electrode snapback on a trace-by-trace basis.[24,36,51] Clear differences in the 2D histograms emerge when they are sorted by measured snapback. Using prior correlation of

electrode structure to snapback, we distinguish measured conductance characteristics for sharp and blunt electrode structures. Motivated by these results, the DFT based calculations address these two scenarios through different model junction structures.

Overall, the group 8 metallocenes form single molecule junctions directly, without the need for traditional linker groups. At 5 K, molecular plateaus with **1** and **2** reproducibly occur in 40-50% of junctions and result in reproducible conductance signatures both during the push and pull portions of the break junction experiment. Interestingly, the conductance measured on all electrode structures is similar, indicating that transport through metallocene molecular junctions formed without linkers is robust and insensitive to the tip structure. The DFT based calculations corroborate this outlook, showing similar junction binding energies for both the sharp and blunt electrode scenarios. Furthermore, the computed trajectories show clear conductance plateaus with a similar magnitude of conductance.

However, the in-depth analysis of the 2D histograms sorted by snap back distance reveals a more nuanced picture with characteristics that do depend on electrode structure, particularly during the push portion of the conductance traces. On average, during all measured pull traces as well as push traces with sharp electrodes, junctions form, persist and then rupture over a displacement distance of about 2 Å, roughly equal to an Au-C donor-acceptor bond. This suggests formation of a specific junction motif with a metal-molecule bond that distorts and then ruptures. A minority of junctions may involve more complex kinetic processes and changes in structure that contribute to longer plateaus. However, on pushing blunt electrodes together, we find that the metallocene molecules, ~3.5 Å in length, can form and maintain a junction with approximately constant conductance for over ~8 Å. Evidently, the molecule bound between blunt electrodes can rotate to accommodate a shortening distance without losing contact. At sufficiently close approach, the

direct tunneling channel between the electrodes, scaled by the area dictated by the blunt electrode structure, rises in importance and ultimately dominates as the electrode separation tends to zero.

The DFT based calculations show that the varied junction scenarios derive from distinct modes of Cp-Au interaction driven by the electron rich π-system on the rings and the barrel shape of the molecule. In the presence of under coordinated Au sites, specific C-Au donor-acceptor bonds form. An alternative scenario in which Au tip atoms directly coordinate the central group A metal atom may also play a role, although it would likely be restricted to a few tip atom structures that can minimize steric hinderance with the rims of the Cp rings. When local flat, close-packed Au patches are available, non-specific binding occurs, involving some electron transfer and further stabilized by stronger Van der Waals interactions between the flat Cp ring and the surface.

These distinct bonding motifs translate to understanding the persistence of the molecular plateaus in the conductance trace of the barrel shaped metallocenes. Typically, "rod" shaped molecular wires bound through amines or thiols display a robust conductance signatures with extended conductance plateaus during pulling because such molecules can bind higher up on a protruding electrode and then change attachment point as the junction is stretched while the conductance is relatively unchanged.[24,50] The flexible link motif adapts to bond to undercoordinated Au atoms along the side of the electrode. For the metallocenes, the electron-rich Cp rings can also form specific donor-acceptor C-Au bonds, but they are much less flexible. The repulsion from the electron-deficient sides of the barrel-shape metallocenes (Fig. 1A) limits binding higher up on an Au electrode. Overall, this binding motif only supports relatively short (~2 Å) plateaus during pulling or pushing. On the other hand, the extended, flat electron-rich Cp surface promotes binding on blunt electrode patches. Our analysis and calculations demonstrate how this binding motif provides an alternative scenario for extended molecular conductance

plateaus. In particular, a tilted molecule can still maintain overlap between the π electrons in the Cp ring and the Au electrode during pushing in this case.

More broadly, our results suggest that the 3D configuration and chemical details of the molecule, which can be synthetically manipulated, relative to the binding site have a defining effect on the selective formation and persistence of molecular junction. In particular, the metallocene substrate can be functionalized in many ways.[7,14,27] This offers the opportunity to manipulate the basic driving forces identified in our work to direct junction formation and tune conductance. Given the role of van der Waals interactions in the persistent conductance plateaus on flat electrodes, the π system of the molecular "barrel" could be expanded to further promote preferential blunt electrode binding by changing the Cp to an indenyl, for example.[71] Alternatively, functionalization of the Cp rings with electron withdrawing or donating substituents can tune the direction of charge transfer between the molecule and the electrode, affecting bonding and transport properties. It can also influence the relative importance of HOMO versus LUMO mediated conductance. Finally, such substituents could also further discourage molecular sliding along the Au electrode due to steric effects. These considerations have implications for future conductance measurements of organometallic and coordination complexes in single molecule junctions.

CONCLUSION

Our results here provide an atomically resolved picture of the binding geometry, charge transfer processes and dynamics of the metallocenes-Au interface. Our break junction conductance measurement protocol combined with density functional theory calculations of junction electronics and geometries allows us to probe the evolution of metallocene-metal junctions which we find to be distinct from most molecules studied to date. The electron rich Cp ring on these organometallic

"barrel" complexes, forms direct bonds to Au electrodes without the need for additional linker groups. We find that the formation and evolution of these junctions is dictated by the electron-rich ring binding sites and the atomic-scale shape of the metal electrodes. Specifically, the formation of specific C-Au donor-acceptor bonds does occur on sharp electrodes but is less energetically favorable than the van der Waals assisted binding of the Cp rings to blunt electrodes where more π overall can occur. Critically, we find that the barrel molecule shape is not compatible with the changing attachment point junction evolution scenario common for rod-like molecules. Instead, persistent plateaus occur on the blunt electrodes where the bulky molecule can tilt and still maintain electric contact with the electrodes through van der Waals interactions.

The picture of junction formation for the barrel shaped molecules identified in this work is distinct from that for much more widely studied, rod shaped molecular wires. It offers interesting opportunities to further manipulate the formation of single molecule junctions that incorporate transition metal atom and tune the conductance characteristics.

Corresponding Author

* Maria Kamenetska; orcid.org/0000-0002-0390-035X; Email: mkamenet@bu.edu

* Mark S. Hybertsen; orcid.org/ 0000-0003-3596-9754; Email: mhyberts@bnl.gov

Author Contributions

The manuscript was written through contributions of all authors. All authors have given approval to the final version of the manuscript.

Supporting Information

Clean Au STMBJ measurements, data filtering details and results, characterization of STMBJ data, room temperature STMBJ measurements, density functional theory data.

Acknowledgement

This research used resources of the Center for Functional Nanomaterials (CFN), which is a U.S. Department of Energy Office of Science User Facility, at Brookhaven National Laboratory under Contract No. DE-SC0012704. This work was supported by the Air Force Office of Scientific Research Young Investigator Research Program, grant no. FA9550-19-1-0224.

REFERENCES

(1) Tanaka, Yuya; Kiguchi, Manabu; Akita, Munetaka. Inorganic and Organometallic Molecular Wires for Single-Molecule Devices. *Chem. - A Eur. J.* **2017**, *23* (20), 4741–4749. https://doi.org/10.1002/chem.201604812.

(2) Higgins, Simon J.; Nichols, Richard J. Metal/Molecule/Metal Junction Studies of Organometallic and Coordination Complexes; What Can Transition Metals Do for Molecular Electronics? *Polyhedron* **2018**, *140*, 25–34. https://doi.org/10.1016/j.poly.2017.10.022.

(3) Bock, Sören; Al-Owaedi, Oday A.; Eaves, Samantha G.; Milan, David C.; Lemmer, Mario; Skelton, Brian W.; Osorio, Henrry M.; Nichols, Richard J.; Higgins, Simon J.; Cea, Pilar; Long, Nicholas J.; Albrecht, Tim; Martín, Santiago; Lambert, Colin J.; Low, Paul J. Single-Molecule Conductance Studies of Organometallic Complexes Bearing 3-Thienyl Contacting Groups. *Chem. - A Eur. J.* **2017**, *23* (9), 2133–2143. https://doi.org/10.1002/chem.201604565.

(4) Liu, Zhen Fei; Wei, Sujun; Yoon, Hongsik; Adak, Olgun; Ponce, Ingrid; Jiang, Yivan; Jang, Woo Dong; Campos, Luis M.; Venkataraman, Latha; Neaton, Jeffrey B. Control of Single-Molecule Junction Conductance of Porphyrins via a Transition-Metal Center. *Nano Lett.* **2014**, *14* (9), 5365–5370. https://doi.org/10.1021/nl5025062.

(5) Getty, Stephanie A.; Engtrakul, Chaiwat; Wang, Lixin; Liu, Rui; Ke, San Huang; Baranger, Harold U.; Yang, Weitao; Fuhrer, Michael S.; Sita, Lawrence R. Near-Perfect Conduction through a Ferrocene-Based Molecular Wire. *Phys. Rev. B - Condens. Matter Mater. Phys.* **2005**, *71* (24), 2–5. https://doi.org/10.1103/PhysRevB.71.241401.

(6) García-Suárez, Víctor M.; Ferrer, Jaime; Lambert, Colin J. Electronic Properties of Metallocene Wires. *Proc. 2006 Int. Conf. Nanosci. Nanotechnology, ICONN* **2006**, 43–45. https://doi.org/10.1109/ICONN.2006.340545.

(7) Farzadi, Roghayeh; Milani Moghaddam, Hossain; Farmanzadeh, Davood. Tuning the Spin Transport Properties of Ferrocene-Based Single Molecule Junctions by Different Linkers. *Chem. Phys. Lett.* **2018**, *704*, 37–44. https://doi.org/10.1016/j.cplett.2018.05.037.

(8) Broadnax, Angela D.; Lamport, Zachary A.; Scharmann, Ben; Jurchescu, Oana D.; Welker, Mark E. Ferrocenealkylsilane Molecular Rectifiers. *J. Organomet. Chem.* **2018**, *856*, 23–26. https://doi.org/10.1016/j.jorganchem.2017.12.019.

(9) Li, Yueqi; Wang, Hui; Wang, Zixiao; Qiao, Yanjun; Ulstrup, Jens; Chen, Hong-Yuan; Zhou, Gang; Tao, Nongjian. Transition from Stochastic Events to Deterministic Ensemble Average in Electron Transfer Reactions Revealed by Single-Molecule Conductance Measurement. *Proc. Natl. Acad. Sci.* **2019**, *116* (9), 3407–3412.

https://doi.org/10.1073/pnas.1814825116.

(10) Uehara, Tomoki; Belosludov, Rodion V.; Farajian, Amir A.; Mizuseki, Hiroshi; Kawazoe, Yoshiyuki. Electronic and Transport Properties of Ferrocene: Theoretical Study. *Japanese J. Appl. Physics, Part 1 Regul. Pap. Short Notes Rev. Pap.* **2006**, *45* (4 B), 3768–3771. https://doi.org/10.1143/JJAP.45.3768.

(11) Xiao, Xiaoyin; Brune, Daniel; He, Jin; Lindsay, Stuart; Gorman, Christopher B.; Tao, Nongjian. Redox-Gated Electron Transport in Electrically Wired Ferrocene Molecules. *Chem. Phys.* **2006**, *326* (1), 138–143. https://doi.org/10.1016/j.chemphys.2006.02.022.

(12) Bredow, T.; Tegenkamp, C.; Pfnür, H.; Meyer, J.; Maslyuk, V. V.; Mertig, I. Ferrocene-1,1′ -Dithiol as Molecular Wire between Ag Electrodes: The Role of Surface Defects. *J. Chem. Phys.* **2008**, *128* (6), 064704. https://doi.org/10.1063/1.2827867.

(13) Lu, Qi; Yao, Chuan; Wang, Xianhong; Wang, Fosong. Enhancing Molecular Conductance of Oligo(p-Phenylene Ethynylene)s by Incorporating Ferrocene into Their Backbones. *J. Phys. Chem. C* **2012**, *116* (33), 17853–17861. https://doi.org/10.1021/jp2119923.

(14) Sun, Yan Yan; Peng, Zheng Lian; Hou, Rong; Liang, Jing Hong; Zheng, Ju Fang; Zhou, Xiao Yi Shun; Zhou, Xiao Yi Shun; Jin, Shan; Niu, Zhen Jiang; Mao, Bing Wei. Enhancing Electron Transport in Molecular Wires by Insertion of a Ferrocene Center. *Phys. Chem. Chem. Phys.* **2014**, *16* (6), 2260–2267. https://doi.org/10.1039/c3cp53269k.

(15) Yu, Jing Xin; Chang, Jing; Wei, Rong Kai; Liu, Xiu Ying; Li, Xiao Dong. Quantum Transport of the Single Metallocene Molecule. *Phys. E Low-Dimensional Syst. Nanostructures* **2016**, *84*, 294–297. https://doi.org/10.1016/j.physe.2016.06.025.

(16) Zhao, Xin; Kastlunger, Georg; Stadler, Robert. Quantum Interference in Coherent Tunneling through Branched Molecular Junctions Containing Ferrocene Centers. *Phys. Rev. B* **2017**, *96* (8), 1–12. https://doi.org/10.1103/PhysRevB.96.085421.

(17) Farzadi, Roghayeh; Milani Moghaddam, Hossain. Greatly Enhanced Spin Filtering of Single Ferrocene Devices: An Ab Initio Study. *Org. Electron.* **2018**, *62* (August), 227–233. https://doi.org/10.1016/j.orgel.2018.08.001.

(18) Ormaza, M.; Abufager, P.; Verlhac, B.; Bachellier, N.; Bocquet, M. L.; Lorente, N.; Limot, L. Controlled Spin Switching in a Metallocene Molecular Junction. *Nat. Commun.* **2017**, *8* (1), 1974. https://doi.org/10.1038/s41467-017-02151-6.

(19) Mohr, Michael; Gruber, Manuel; Weismann, Alexander; Jacob, David; Abufager, Paula; Lorente, Nicolás; Berndt, Richard. Spin Dependent Transmission of Nickelocene-Cu Contacts Probed with Shot Noise. *Phys. Rev. B* **2020**, *101* (7), 75414. https://doi.org/10.1103/PhysRevB.101.075414.

(20) Verlhac, B.; Bachellier, N.; Garnier, L.; Ormaza, M.; Abufager, P.; Robles, R.; Bocquet, M. L.; Ternes, M.; Lorente, N.; Limot, L. Atomic-Scale Spin Sensing with a Single Molecule at the Apex of a Scanning Tunneling Microscope. *Science (80-.).* **2019**, *366* (6465), 623–627. https://doi.org/10.1126/science.aax8222.

(21) Pal, Atindra Nath; Li, Dongzhe; Sarkar, Soumyajit; Chakrabarti, Sudipto; Vilan, Ayelet; Kronik, Leeor; Smogunov, Alexander; Tal, Oren. Nonmagnetic Single-Molecule Spin-Filter Based on Quantum Interference. *Nat. Commun.* **2019**, *10* (1), 1–8. https://doi.org/10.1038/s41467-019-13537-z.

(22) Kamenetska, M.; Koentopp, M.; Whalley, A. C.; Park, Y. S.; Steigerwald, M. L.; Nuckolls, C.; Hybertsen, M. S.; Venkataraman, L. Formation and Evolution of Single-Molecule Junctions. *Phys. Rev. Lett.* **2009**, *102* (12), 126803. https://doi.org/10.1103/PhysRevLett.102.126803.

(23) McNeely, James; Miller, Nicholas; Pan, Xiaoyun; Lawson, Brent; Kamenetska, Maria. Angstrom-Scale Ruler Using Single Molecule Conductance Signatures. *J. Phys. Chem. C* **2020**, *124* (24), 13427–13433. https://doi.org/10.1021/acs.jpcc.0c02063.

(24) Kamenetska, M.; Widawsky, J. R.; Dell'Angela, M.; Frei, M.; Venkataraman, Latha. Temperature Dependent Tunneling Conductance of Single Molecule Junctions. *J. Chem. Phys.* **2017**, *146* (9), 092311. https://doi.org/10.1063/1.4973318.

(25) Yelin, Tamar; Chakrabarti, Sudipto; Vilan, Ayelet; Tal, Oren. Richness of Molecular Junction Configurations Revealed by Tracking a Full Pull-Push Cycle. *Nanoscale* **2021**, *13* (44), 18434–18440. https://doi.org/10.1039/d1nr05680h.

(26) Kanthasamy, Karthiga; Ring, Markus; Nettelroth, Dennes; Tegenkamp, Christoph; Butenschön, Holger; Pauly, Fabian; Pfnür, Herbert. Charge Transport through Ferrocene 1,1′-Diamine Single-Molecule Junctions. *Small* **2016**, *12* (35), 4849–4856. https://doi.org/10.1002/smll.201601051.

(27) Camarasa-Gómez, María; Hernangómez-Pérez, Daniel; Inkpen, Michael S.; Lovat, Giacomo; Fung, E. Dean; Roy, Xavier; Venkataraman, Latha; Evers, Ferdinand. Mechanically Tunable Quantum Interference in Ferrocene-Based Single-Molecule Junctions. *Nano Lett.* **2020**, *20* (9), 6381–6386. https://doi.org/10.1021/acs.nanolett.0c01956.

(28) Zahl, Percy; Klust, Andreas. Gnome X Scanning Microscopy. http://gxsm.sourceforge.net/ (accessed 2022-03-15)

(29) Zahl, Percy; Wagner, Thorsten. GXSM - Smart & Customizable SPM Control. *Imaging & Microscopy (GIT)*. Imaging & Microscopy (GIT) 2015.

(30) Kamenetska, M.; Dell'angela, M.; Widawsky, J. R.; Kladnik, G.; Verdini, A.; Cossaro, A.; Cvetko, D.; Morgante, A.; Venkataraman, L. Structure and Energy Level Alignment of Tetramethyl Benzenediamine on Au(111). *J. Phys. Chem. C* **2011**, *115* (25), 12625–12630. https://doi.org/10.1021/jp202555d.

(31) Braun, K. F.; Iancu, V.; Pertaya, N.; Rieder, K. H.; Hla, S. W. Decompositional Incommensurate Growth of Ferrocene Molecules on a Au(111) Surface. *Phys. Rev. Lett.* **2006**, *96* (24), 1–4. https://doi.org/10.1103/PhysRevLett.96.246102.

(32) Knaak, Thomas; González, César; Dappe, Yannick J.; Harzmann, Gero D.; Brandl, Thomas; Mayor, Marcel; Berndt, Richard; Gruber, Manuel. Fragmentation and Distortion of Terpyridine-Based Spin-Crossover Complexes on Au(111). *J. Phys. Chem. C* **2019**, *123* (7), 4178–4185. https://doi.org/10.1021/acs.jpcc.8b11242.

(33) Skipper, Hannah E.; May, Claire V.; Rheingold, Arnold L.; Doerrer, Linda H.; Kamenetska, Maria. Hard–Soft Chemistry Design Principles for Predictive Assembly of Single Molecule-Metal Junctions. *J. Am. Chem. Soc.* **2021**, *143* (40), 16439–16447. https://doi.org/10.1021/JACS.1C05142.

(34) Quek, Su Ying; Kamenetska, Maria; Steigerwald, Michael L.; Choi, Hyoung Joon; Louie, Steven G.; Hybertsen, Mark S.; Neaton, J. B.; Venkataraman, Latha. Mechanically Controlled Binary Conductance Switching of a Single-Molecule Junction. *Nat. Nanotechnol.* **2009**, *4* (4), 230–234. https://doi.org/10.1038/nnano.2009.10.

(35) Untiedt, C.; Yanson, A. I.; Grande, R.; Rubio-Bollinger, G.; Agraït, N.; Vieira, S.; van Ruitenbeek, J. M. Calibration of the Length of a Chain of Single Gold Atoms. *Phys. Rev. B - Condens. Matter Mater. Phys.* **2002**, *66* (8), 854181–854186. https://doi.org/10.1103/PhysRevB.66.085418.

(36) Trouwborst, M. L.; Huisman, E. H.; Bakker, F. L.; Van Der Molen, S. J.; Van Wees, B. J.

Single Atom Adhesion in Optimized Gold Nanojunctions. *Phys. Rev. Lett.* **2008**, *100* (17), 175502. https://doi.org/10.1103/PhysRevLett.100.175502.

(37) Xu, Bingqian; Tao, Nongjian J. Measurement of Single-Molecule Resistance by Repeated Formation of Molecular Junctions. *Science (80-.).* **2003**, *301* (5637), 1221–1223. https://doi.org/10.1126/science.1087481.

(38) Park, Young S.; Whalley, Adam C.; Kamenetska, Maria; Steigerwald, Michael L.; Hybertsen, Mark S.; Nuckolls, Colin; Venkataraman, Latha. Contact Chemistry and Single-Molecule Conductance: A Comparison of Phosphines, Methyl Sulfides, and Amines. *J. Am. Chem. Soc.* **2007**, *129* (51), 15768–15769. https://doi.org/10.1021/ja0773857.

(39) Leary, Edmund; Zotti, Linda A.; Miguel, Delia; Márquez, Irene R.; Palomino-Ruiz, Lucía; Cuerva, Juan Manuel; Rubio-Bollinger, Gabino; González, M. Teresa; Agrait, Nicolás. The Role of Oligomeric Gold-Thiolate Units in Single-Molecule Junctions of Thiol-Anchored Molecules. *J. Phys. Chem. C* **2018**, *122* (6), 3211–3218. https://doi.org/10.1021/acs.jpcc.7b11104.

(40) Cabosart, Damien; El Abbassi, Maria; Stefani, Davide; Frisenda, Riccardo; Calame, Michel; Van der Zant, Herre S. J.; Perrin, Mickael L. A Reference-Free Clustering Method for the Analysis of Molecular Break-Junction Measurements. *Appl. Phys. Lett.* **2019**, *114* (14), 143102. https://doi.org/10.1063/1.5089198.

(41) Hamill, J. M.; Zhao, X. T.; Mészáros, G.; Bryce, M. R.; Arenz, M. Fast Data Sorting with Modified Principal Component Analysis to Distinguish Unique Single Molecular Break Junction Trajectories. *Phys. Rev. Lett.* **2018**, *120* (1), 016601. https://doi.org/10.1103/PhysRevLett.120.016601.

(42) Lemmer, Mario; Inkpen, Michael S.; Kornysheva, Katja; Long, Nicholas J.; Albrecht, Tim. Unsupervised Vector-Based Classification of Single-Molecule Charge Transport Data. *Nat. Commun. 2016 71* **2016**, *7* (1), 1–10. https://doi.org/10.1038/ncomms12922.

(43) Blum, Volker; Gehrke, Ralf; Hanke, Felix; Havu, Paula; Havu, Ville; Ren, Xinguo; Reuter, Karsten; Scheffler, Matthias. Ab Initio Molecular Simulations with Numeric Atom-Centered Orbitals. *Comput. Phys. Commun.* **2009**, *180* (11), 2175–2196. https://doi.org/10.1016/j.cpc.2009.06.022.

(44) Ren, Xinguo; Rinke, Patrick; Blum, Volker; Wieferink, Jürgen; Tkatchenko, Alexandre; Sanfilippo, Andrea; Reuter, Karsten; Scheffler, Matthias. Resolution-of-Identity Approach to Hartree-Fock, Hybrid Density Functionals, RPA, MP2 and GW with Numeric Atom-Centered Orbital Basis Functions. *New J. Phys.* **2012**, *14,* 053020. https://doi.org/10.1088/1367-2630/14/5/053020.

(45) Arnold, A.; Weigend, F.; Evers, F. Quantum Chemistry Calculations for Molecules Coupled to Reservoirs: Formalism, Implementation, and Application to Benzenedithiol. *J. Chem. Phys.* **2007**, *126* (17), 174101. https://doi.org/10.1063/1.2716664.

(46) Bagrets, Alexei. Spin-Polarized Electron Transport across Metal-Organic Molecules: A Density Functional Theory Approach. *J. Chem. Theory Comput.* **2013**, *9* (6), 2801–2815. https://doi.org/10.1021/ct4000263.

(47) Wilhelm, Jan; Walz, Michael; Stendel, Melanie; Bagrets, Alexei; Evers, Ferdinand. Ab Initio Simulations of Scanning-Tunneling-Microscope Images with Embedding Techniques and Application to C58-Dimers on Au(111). *Phys. Chem. Chem. Phys.* **2013**, *15* (18), 6684–6690. https://doi.org/10.1039/c3cp44286a.

(48) Perdew, John P.; Burke, Kieron; Ernzerhof, Matthias. Generalized Gradient

Approximation Made Simple. *Phys. Rev. Lett.* **1996**, *77* (18), 3865–3868. https://doi.org/10.1103/PhysRevLett.77.3865.

(49) Tkatchenko, Alexandre; Scheffler, Matthias. Accurate Molecular van Der Waals Interactions from Ground-State Electron Density and Free-Atom Reference Data. *Phys. Rev. Lett.* **2009**, *102* (7), 6–9. https://doi.org/10.1103/PhysRevLett.102.073005.

(50) Li, Haipeng B.; Xi, Yan-Feng; Hong, Ze-Wen; Yu, Jingxian; Li, Xiao-Xia; Liu, Wen-Xia; Domulevicz, Lucas; Jin, Shan; Zhou, Xiao-Shun; Hihath, Joshua. Temperature-Dependent Tunneling in Furan Oligomer Single-Molecule Junctions. *ACS Sensors* **2021**, 0–7. https://doi.org/10.1021/acssensors.0c02278.

(51) Yanson, A. I.; Rubio Bollinger, G.; Van Den Brom, H. E.; Agraït, N.; Van Ruitenbeek, J. M. Formation and Manipulation of a Metallic Wire of Single Gold Atoms. *Nature* **1998**, *395* (6704), 783–785. https://doi.org/10.1038/27405.

(52) Agraït, Nicolás; Yeyati, Alfredo Levy; van Ruitenbeek, Jan M. Quantum Properties of Atomic-Sized Conductors. *Phys. Rep.* **2003**, *377* (2–3), 81–279. https://doi.org/10.1016/S0370-1573(02)00633-6.

(53) Ohnishi, Hideaki; Kondo, Yukihito; Takayanagi, Kunio. Quantized Conductance through Individual Rows of Suspended Gold Atoms. *Nature* **1998**, *395* (6704), 780–783. https://doi.org/10.1038/27399.

(54) Rodrigues, Varlei; Fuhrer, Tobias; Ugarte, Daniel. Signature of Atomic Structure in the Quantum Conductance of Gold Nanowires. *Phys. Rev. Lett.* **2000**, *85* (19), 4124. https://doi.org/10.1103/PhysRevLett.85.4124

(55) Li, Shi; Jiang, Yuxuan; Wang, Yongfeng; Hou, Shimin. The Formation and Conducting Mechanism of Imidazole-Gold Molecular Junctions. *ChemistrySelect* **2021**, *6* (12), 2959–2965. https://doi.org/10.1002/slct.202100507.

(56) Hines, Thomas; Diez-Perez, Ismael; Hihath, Joshua; Liu, Hongmei; Wang, Zhong-Sheng; Zhao, Jianwei; Zhou, Gang; Müllen, Klaus; Tao, Nongjian. Transition from Tunneling to Hopping in Single Molecular Junctions by Measuring Length and Temperature Dependence. *J. Am. Chem. Soc.* **2010**, *132* (33), 11658–11664. https://doi.org/10.1021/JA1040946.

(57) Leary, E.; Höbenreich, H.; Higgins, S. J.; Zalinge, H. van; Haiss, W.; Nichols, R. J.; Finch, C. M.; Grace, I.; Lambert, C. J.; McGrath, R.; Smerdon, J. Single-Molecule Solvation-Shell Sensing. *Phys. Rev. Lett.* **2009**, *102* (8), 086801. https://doi.org/10.1103/PhysRevLett.102.086801.

(58) Sohn, Y. S.; Hendrickson, D. N.; Gray, H. B. Electronic Structure of Ferricenium Ion Sir: *J. Am. Chem. Soc.* **1970**, *92* (10), 3233–3234.

(59) Yamaguchi, Yoshikazu; Ding, Wei; Sanderson, Cynthia T.; Borden, Michelle L.; Morgan, Matthew J.; Kutal, Charles. Electronic Structure, Spectroscopy, and Photochemistry of Group 8 Metallocenes. *Coord. Chem. Rev.* **2007**, *251* (3–4), 515–524. https://doi.org/10.1016/j.ccr.2006.02.028.

(60) Atkins, Andrew J.; Bauer, Matthias; Jacob, Christoph R. The Chemical Sensitivity of X-Ray Spectroscopy: High Energy Resolution XANES versus X-Ray Emission Spectroscopy of Substituted Ferrocenes. *Phys. Chem. Chem. Phys.* **2013**, *15* (21), 8095–8105. https://doi.org/10.1039/c3cp50999k.

(61) Haaland, Arne. Molecular Structure and Bonding in the 3d Metallocenes. *Acc. Chem. Res.* **1979**, *12* (11), 415–422. https://doi.org/10.1021/ar50143a006.

(62) Bean, David E.; Fowler, Patrick W.; Morris, Michael J. Aromaticity and Ring Currents in

Ferrocene and Two Isomeric Sandwich Complexes. *J. Organomet. Chem.* **2011**, *696* (10), 2093–2100. https://doi.org/10.1016/j.jorganchem.2010.11.014.

(63) Ormaza, Maider; Abufager, Paula; Bachellier, Nicolas; Robles, Roberto; Verot, Martin; Le Bahers, Tangui; Bocquet, Marie Laure; Lorente, Nicolas; Limot, Laurent. Assembly of Ferrocene Molecules on Metal Surfaces Revisited. *J. Phys. Chem. Lett.* **2015**, *6* (3), 395–400. https://doi.org/10.1021/jz5026118.

(64) Bachellier, N.; Ormaza, M.; Faraggi, M.; Verlhac, B.; Vérot, M.; Le Bahers, T.; Bocquet, M. L.; Limot, L. Unveiling Nickelocene Bonding to a Noble Metal Surface. *Phys. Rev. B* **2016**, *93* (19), 1–6. https://doi.org/10.1103/PhysRevB.93.195403.

(65) Toher, C.; Filippetti, A.; Sanvito, S.; Burke, Kieron. Self-Interaction Errors in Density-Functional Calculations of Electronic Transport. *Phys. Rev. Lett.* **2005**, *95* (14), 1–4. https://doi.org/10.1103/PhysRevLett.95.146402.

(66) Koentopp, Max; Burke, Kieron; Evers, Ferdinand. Zero-Bias Molecular Electronics: Exchange-Correlation Corrections to Landauer's Formula. *Phys. Rev. B - Condens. Matter Mater. Phys.* **2006**, *73* (12), 1–4. https://doi.org/10.1103/PhysRevB.73.121403.

(67) Ke, San Huang; Baranger, Harold U.; Yang, Weitao. Role of the Exchange-Correlation Potential in Ab Initio Electron Transport Calculations. *J. Chem. Phys.* **2007**, *126* (20), 201102. https://doi.org/10.1063/1.2743004.

(68) Quek, Su Ying; Venkataraman, Latha; Choi, Hyoung Joon; Louie, Steven G.; Hybertsen, Mark S.; Neaton, J. B. Amine - Gold Linked Single-Molecule Circuits: Experiment and Theory. *Nano Lett.* **2007**, *7* (11), 3477–3482. https://doi.org/10.1021/nl072058i.

(69) Evers, Ferdinand; Korytár, Richard; Tewari, Sumit; Van Ruitenbeek, Jan M. Advances and Challenges in Single-Molecule Electron Transport. *Rev. Mod. Phys.* **2020**, *92* (3), 35001. https://doi.org/10.1103/RevModPhys.92.035001.

(70) Fatemi, V.; Kamenetska, M.; Neaton, J. B.; Venkataraman, L. Environmental Control of Single-Molecule Junction Transport. *Nano Lett.* **2011**, *11* (5), 1988–1992.

(71) Nguyen, Khiem T.; Lane, Emily E.; McMillen, Colin D.; Pienkos, Jared A.; Wagenknecht, Paul S. Is Indenyl a Stronger or Weaker Electron Donor Ligand than Cyclopentadienyl? Opposing Effects of Indenyl Electron Density and Ring Slipping on Electrochemical Potentials. *Organometallics* **2020**, *39* (5), 670–678. https://doi.org/10.1021/ACS.ORGANOMET.9B00818.

For Table of Contents Only